Since January 2020 Elsevier has created a COVID-19 resource centre with free information in English and Mandarin on the novel coronavirus COVID-19. The COVID-19 resource centre is hosted on Elsevier Connect, the company's public news and information website.

11

COVID-19–affected medical image analysis using DenserNet

Chandranath Adak[1], Debmitra Ghosh[1], Ranjana Roy Chowdhury[2], Soumi Chattopadhyay[2]

[1]CENTRE FOR DATA SCIENCE, JIS INSTITUTE OF ADVANCED STUDIES AND RESEARCH, JIS UNIVERSITY, KOLKATA, WEST BENGAL, INDIA; [2]DEPARTMENT OF CSE, INDIAN INSTITUTE OF INFORMATION TECHNOLOGY GUWAHATI, ASSAM, INDIA

1. Introduction

The 2019–20 coronavirus pandemic is the biggest threat that the world is facing today. The coronavirus outbreak was first identified in Wuhan, China, in December 2019 [1]. The World Health Organization (WHO) declared the outbreak as a "public health emergency of international concern" on January 30, 2020, and a "pandemic" on March 11, 2020 [2,3]. The disease caused by Severe Acute Respiratory Syndrome CoronaVirus-2 (SARS-CoV-2) is named as COVID-19 [1], which is coined from the term COronaVIrus Disease, and 19 stands for 2019 since it was first identified in December 2019 in Wuhan, China. It was previously referred to as the novel CoronaVirus or 2019-nCoV by WHO [2,3].

The symptoms of the coronavirus disease are quite common to cold, which include fever, sore throat, dry cough, fatigue, shortness of breath, loss of smell, etc. Therefore, observing the symptoms, it is quite difficult to distinguish the disease from normal or seasonal flu. Moreover, the coronavirus is highly contiguous and is primarily spread from the close-contact between people, often through small droplets produced by sneezing, coughing, or talking [1,3]. It has also been observed that people may become affected by touching a contaminated surface, followed by touching their faces. Therefore, the rapid growth of the virus is noted across the world. As of April 29, 2020, more than 3.19 million cases of COVID-19 have been reported across 185 countries, where the world has witnessed about 2,27,000 death cases [4]. Fig. 11.1a–c show the worldwide cumulative affected cases, death cases, and country-wise death percentages, respectively. From Fig. 11.1a, it can be easily observed that the COVID-19–affected cases are increasing exponentially.

To prevent the spread of the disease, the detection of this disease is utterly important. However, the testing of this disease is facing an unprecedented challenge. On one hand, as of now (April 29, 2020), this disease is almost impossible to detect from its symptoms.

Data Science for COVID-19. https://doi.org/10.1016/B978-0-12-824536-1.00021-6

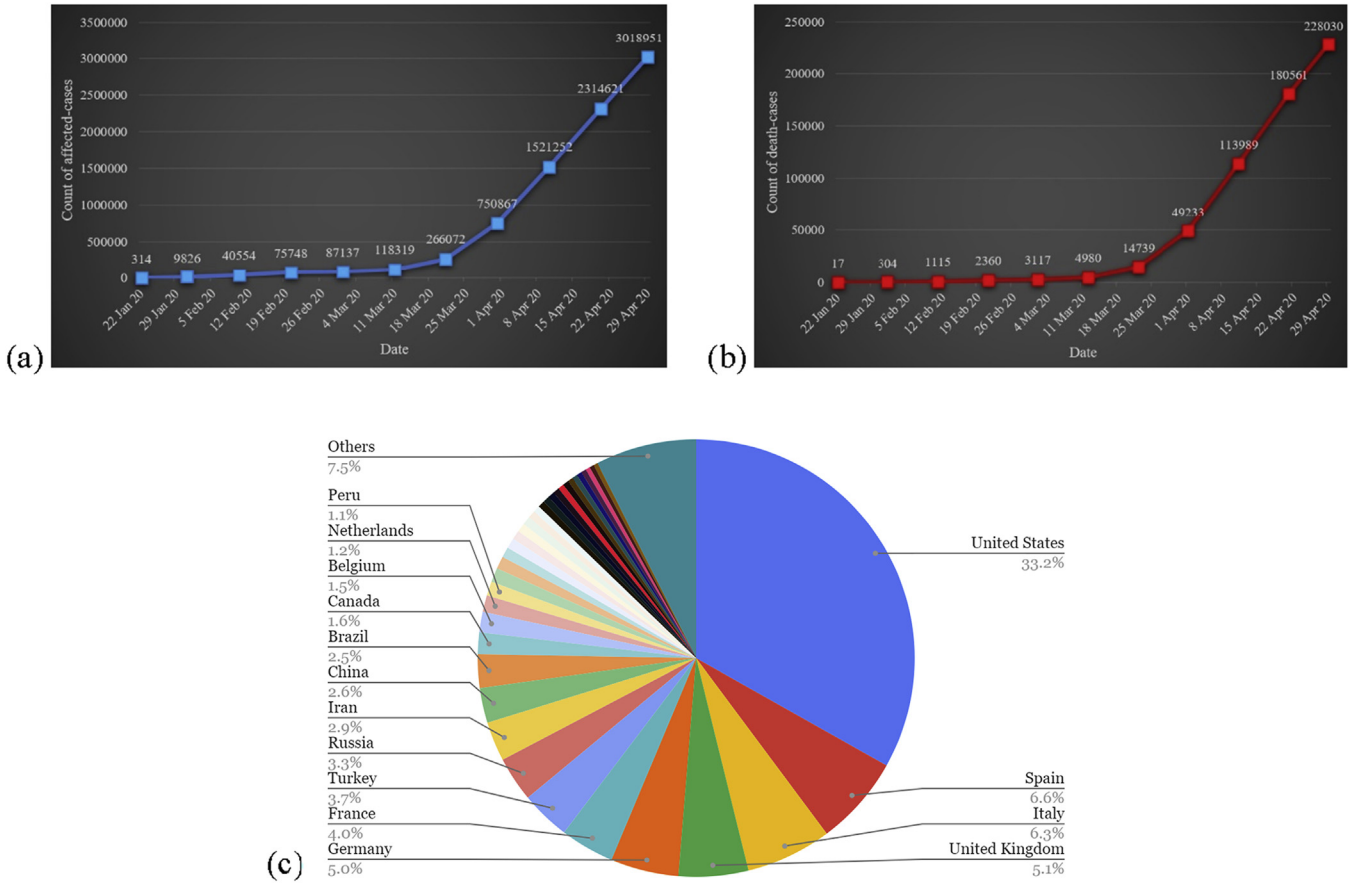

FIGURE 11.1 Worldwide COVID-19 spread: (a) cumulative number of affected cases, (b) cumulative number of death cases, and (c) country-wise death percentage. *Data collected up to April 29, 2020 from* Worldwide Coronavirus Dashboard*: https://covid-019.com.*

On the other hand, providing the testing infrastructure considering the massive spread rate of this disease is becoming nearly infeasible. Moreover, because of the infectious nature of the disease, medical experts are also getting infected by this disease while treating the patients. The major problems with conventional diagnostic strategies are as follows:

- The diagnosis is a time-consuming approach.
- Infrastructure required to store specimens: special biosafety lab is required to store a polymerase chain reaction (PCR) machine, which is very costly.
- Shortage of testing-kits: sufficient test kits are not available considering the requirement to test this disease. Moreover, a reverse transcriptase (RT)-PCR kit does not cost-efficient.
- A phlebotomist is required for testing purposes, who is getting exposed to invasive swab.
- The testing is prone to human error and bias to a cost-effective approach.

Considering the above problems, an alternate coronavirus detection strategy can be very useful along with the conventional testing mechanism. Other methods of diagnosis include clinical approach, medical image (computed tomography (CT) or chest X-ray) analysis, pathogenic test, etc. In this paper, we aim to analyze COVID-19 at an early stage of infection by leveraging chest X-ray and CT scan images.

The use of chest X-ray and CT scan images are very common in medical image processing to diagnose various kind of diseases. CT [5–7] is an X-ray measurement obtained from diverse angles to generate cross-sectional images of certain regions of a scanned object, which allows the user to inspect inside the object without any surgery. Magnetic resonance imaging (MRI) [8–13] is another medical imaging technique used to form pictures of the anatomy using nuclear magnetic resonance. Recently, radiography images are also becoming popular [14], where the image capturing systems are equipped with digital sensors that use X-rays, gamma rays, or similar ionizing/nonionizing radiation to reflect the internal view of an object. In the field of medical image analysis, various computer vision techniques (e.g., segmentation [15,16], slicing [17–19], clustering [9,20]) have shown to be very effective and played a crucial role in the early detection of major diseases in the brain, kidney, breast, prostate, etc. [21,22]. For example, diagnosis of heart diseases [23], tumor detection [24], bone fracture finding [25], bone age prediction [26], etc., are carried out by analyzing medical images.

In this paper, we propose a new architecture to analyze the COVID-19–affected medical images. Our proposed method (say, DenserNet) uses the densely connected convolution neural network. The proposed DenserNet is an improvement over the DenseNet [27]. For experimental analysis, we employ two public databases containing chest X-ray and CT-scan images. The experimental results are quite encouraging.

Our contribution to this paper is of two folds comprising a novel solution architecture proposal and its application on COVID-19 study.

- ***Solution architecture:*** We propose a new architecture (DenserNet) to tackle the general classification problem. This architecture is an improvisation of the DenseNet [27].
- ***Application:*** We propose a framework to analyze medical images, especially X-ray and CT scan images to expedite the study of COVID-19–affected cases.

This paper is organized as follows. Section 2 discusses the related works on medical image analysis. Then Section 3 formulates the undertaken research problem. The proposed methodology is given in Section 4. The experimental results are presented in Section 5. Finally, Section 6 concludes this paper.

2. Related works

The medical image processing has acquired great attention in the field of health care since the day digital images came into existence. Some common medical digital imagings are CT [5–7], MRI [8–13], etc. Along with these digital imagings, the recent addition of an analog imaging modality, i.e., radiography [14] equipped with digital sensors, has attracted significant research attention. Many works have been performed using digital images to address several problems of the medical domain [21,28,29].

With the alliance of medical imaging and computer vision, many successful works have been proposed in the medical domain, which has played a significant role to perform early identification of major diseases related to the brain, chest, breast, kidney, prostate, and many other organs. Taking assistance from computer vision, the medical image analysis explores various facets, such as segmentation [15,16,29,30], slicing [17–19], clustering [9,20], acuity [21], etc., for a better view of the subsections with a detailed study. Segmentation [29] of an image into small subsections provides a better view of remote sections. Each subsection contains minute information that is subjected to further processing for information extraction. Often the digital images used in medical science come out to be blurry or having a blunt outline. The quality of images is also sometimes not up to the mark because of which processing becomes tough. Subsequently, the accurate localization of complex boundaries of various tiny isolated parts cannot be performed properly. Kruggel [21] dealt with the quality of digital images by taking the acuity measure and the statistical properties of images. Zhou et al. [29] addressed this problem by exploiting the basic information of the images for a better understanding of the outlines and subsections. They took into account the semantic information of the images for accurate boundary localization.

For extracting the features and some other latent information from images, deep learning has played a remarkable role in the field of medical sciences. The convolutional neural network (CNN) has been an important part of analyzing the visual imagery. A decent amount of research works [22,29,31] employed deep learning–based approaches and extracted useful information from the medical images. The deep learning–based models are usually dependent on huge training data, but sometimes the availability of sufficient distinct images for training is not available. To deal with this

issue, Zhang et al. [22] implemented a two-stage task-oriented deep learning method for finding large-scale anatomical landmarks simultaneously in real-time with limited training data.

For the extraction of fine patterns and features in a medical image, another kind of method involves the slicing [17,18] of images. Slicing often creates fine pieces of an image from various positions so that a diverse view of the image can be obtained for additional processing. Manojlovic et al. [20] dealt with radiology images and dynamically sliced it for further processing of images.

With the outbreak of COVID-19 pandemic, multiple research works are being carried to detect the possibilities of positive cases and also to find solutions to its recovery. Medical images of the COVID-19–affected patients have been taken into account to study the patients. One such convenient medical image is the chest X-ray image of COVID-19–affected patient, which has been widely used for predictions and classification of positive and nonpositive cases. The combination of medical sciences with computer vision has helped to an extent in figuring out the positive cases of COVID-19. Multiple works [32–36] have been done on COVID-19 by considering the CT scans and chest X-ray images of COVID-19–affected patients. Most of the studies have employed deep learning techniques [31,32,34,37–39] supported by CNNs for the detection of COVID-19 cases with respect to the chest X-ray images. To determine the COVID-19 positive cases, the task is mostly modeled into a supervised classification [33,40] of medical images. However, the deep learning techniques are dependent on the training data, for which sufficient data supply is required to train the model properly. Because of the inaccessibility of a sufficient amount of data, it becomes difficult to train the model. This problem can be handled by the transfer learning technique, which allows using the knowledge gathered from some other computer vision tasks. The studies reported in Refs. [36,41] employed transfer learning to address the problem of insufficient data and analyzed the COVID-19 positive cases concerning X-ray and CT scan images. However, there is a scope of improvement over the past works [42] concerning the accuracy, which we address in this paper.

3. Problem formulation

In this section, we formulate the problem considered in this paper.

Our framework is an analysis framework, where we have a medical image database. This database contains multiple labeled chest X-ray and CT scan images of various classes. Such an image is the input to the framework. The problem is formulated as a supervised classification task and includes the following analyses:

- We first formulate our problem as a binary classification task, where the objective is to identify COVID-19 versus non-COVID-19 medical images.
- We further concentrate on more granular classification and formulate a multiclass classification problem. The objective of this problem is to categorize the medical images into classes like normal, bacteria, viral COVID-19, viral non-COVID-19, etc.

Primarily, we create a trained model based on the training set. After the proper training, the trained model can be used to predict the class of an unlabeled image. Thus, a chest X-ray/CT scan image can be analyzed whether the patient is COVID-19–affected or not. More details regarding the research tasks undertaken in this paper can be found in Section 5.2.

4. Proposed methodology

In this section, we discuss our proposed method. This research emphasizes the classification task. Therefore, we propose a novel architecture that can handle the classification problem.

In a deep convolutional architecture [43], an image is fed to the system and usually passed through a sequence of layers. The input image transforms through every layer l, which comprises nonlinear transformation G_l. This G_l is a composite function of multiple operations, such as batch normalization (BN) [44], activation function (e.g., ReLU) [45], and convolution [43,45], or pooling [43,45], etc. The output of the lth layer is denoted as x_l.

Convolutional neural network: In the traditional CNN [43], during feed-forward connection, the input of the lth layer is the output of the previous $(l-1)$th layer, which can be written as below.

$$x_l = G_l(x_{l-1}) \tag{11.1}$$

ResNet: The residual network (ResNet) [46] adds a skip connection besides the main feed-forward connection, which utilizes the residues of the previous layer. This is represented as follows:

$$x_l = G_l(x_{l-1}) + x_{l-1} \tag{11.2}$$

In ResNet, the skip connection (output of G_l) and the main identity connection (x_{l-1}) is combined with a summation/linear transformation, which may lead to some information loss [27]. Therefore, instead of summation, concatenation can be used.

Dense connection: In a dense convolutional network (DenseNet) [27], besides introducing the concatenation idea, the information flow between layers is improved. In DenseNet, multiple dense blocks are linked sequentially with the transition layers comprising convolution and pooling operations. Inside a dense block, the connection is *dense*, where the feature map of the lth layer (x_l) is dependent on all the feature maps of all the preceding layers, i.e., x_0, x_1, …, x_{l-1}. It can be denoted as follows.

$$x_l = G_l([x_0, x_1, \dots, x_{l-1}]) \tag{11.3}$$

where $[x_0, x_1, \dots, x_{l-1}]$ is the concatenation of the feature maps obtained from layers $0, 1, \dots, l-1$, and G_l is a composite function.

DenserNet: We adopt the idea of a dense block in our proposed architecture. We pictorially present the internal view of a dense block in Fig. 11.2 that is used in our architecture, where the dense connectivity among layers can be observed. The main

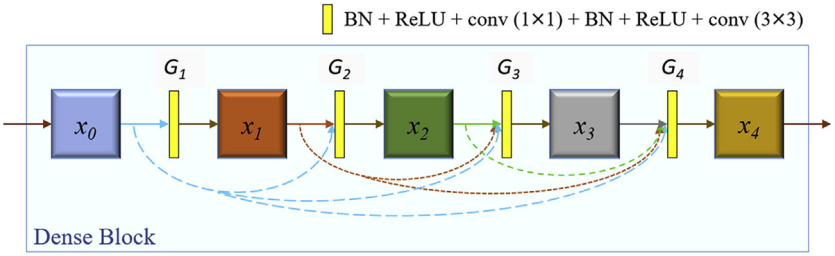

FIGURE 11.2 Internal view of a Dense Block.

connections are shown by horizontal rigid lines, whereas the skip connections are shown using dotted lines. The composite function G_l comprises six successive operations, i.e., BN, Rectified Linear Unit (ReLU) activation, 1×1 convolution (conv), followed by BN, ReLU, 3×3 conv. In a dense block, x_0 is the input feature map, and x_l is the output feature map. In Fig. 11.2, $l = 4$.

In DenseNet, the dense connection is only present inside a dense block, i.e., *intra* dense block connection [27]. We propose an architecture, where besides the intra-dense block connection, additional dense connections exist among the dense blocks, i.e., *inter*-dense block connection. Therefore, our proposed architecture is *denser* than DenseNet. We coin the name "DenserNet" to refer to our architecture.

Our DenserNet architecture contains multiple dense blocks. Here, all the dense blocks are similar, i.e., each has the same l number of layers. In a dense block, the number of channels of input and output feature maps is kept the same. Therefore, for simplicity, all the feature maps inside a dense block contain the same number of channels. For example, in Fig. 11.2, if the input feature map x_0 contains n_c number of channels, then the output feature map x_4, and in-between feature maps x_1, x_2, x_3 also contain n_c number of channels, individually.

In Fig. 11.3, we graphically present a generalized version of our DenserNet architecture. The output of the mth dense block is d_m, which is actually the last feature map of the mth dense block.

The input of the $(m+1)$th dense block is a feature map f_m. The f_m is a concatenation of multiple feature maps, calculated as follows.

$$f_m = \left[Q_m^1(d_m), Q_m^2(d_{m-1}), Q_m^3(d_{m-2}), \ldots, Q_m^m(d_1)\right] \tag{11.4}$$

where Q_m^i is a composite function applied after the mth dense block.

Q_m^i contains four consecutive operations, BN, ReLU, 1×1 convolution (conv), and $2^i \times 2^i$ max pooling (pool) layers; $\forall\, i = 1, 2, \ldots, m$, and $m \geq 1$. The input and output feature maps of Q_m^i consist of the same number of channels.

The main connection contains composite functions Q_m^i, for $i = 1$. As a matter of fact, the main connection comprises only $2^1 \times 2^1$ max-pooling layers.

In Fig. 11.3, $m = 4$. Here also, we show the main connection with rigid lines, and the skip connections with dotted lines.

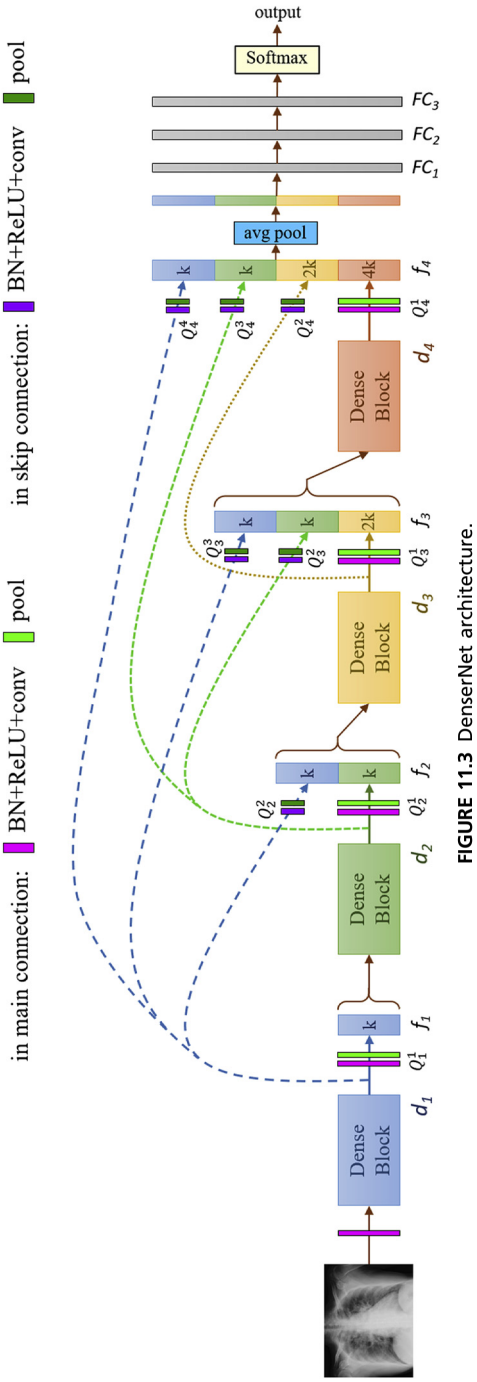

FIGURE 11.3 DenserNet architecture.

Input: An image is fed to our DenserNet architecture. The image is then transformed using a composite function containing BN, ReLU, and 1×1 conv. Here, during the convolution, we employ k number of filters to obtain a feature map with k channels. The transformed output is fed to the first dense block. Therefore, the first feature map of the first dense block consists of a k channeled feature map.

Growth rate: The input and output feature maps of a dense block contain the same number of channels. The composite function Q_m^i also maintains the same number of channels. After the operation of the first dense block, the number of channels of feature map f_1 is k. The value of k grows with the number of dense blocks because of concatenation. As a matter of fact, f_2 has $2k$ channels obtained after the execution of the second dense block, f_3 contains $4k$ channels attained after the operation of the third block, and so on. In this manner, after the execution of the m^{th}th block, f_m consists $2^{m-1}k$ number of channels. Here, k is a hyper-parameter, which grows with the number of dense blocks.

We present an example concerning Fig. 11.3 and Eq. (11.4) as follows:

$$f_4 = \left[Q_4^1(d_4), Q_4^2(d_3), Q_4^3(d_2), Q_4^4(d_1)\right] \tag{11.5}$$

The feature map f_4 is a concatenation of $4k$, $2k$, k, and k channeled features maps obtained from $Q_4^1(d_4)$, $Q_4^2(d_3)$, $Q_4^3(d_2)$, and $Q_4^4(d_1)$, respectively. Therefore, f_4 contains a total of $8k\left(=4k+2k+k+k=2^{4-1}k\right)$ number of channels.

Classification: The f_m is passed through a global average pooling (avg pool) layer that produces $2^{m-1}k$ channeled feature maps, each of size 1×1. We flatten this feature map and generate a linear representation of a feature vector with dimension $2^{m-1}k$. This flattened layer (FC_1) with $2^{m-1}k$ number of nodes is fully connected to a successive layer (FC_2) that contains h number of nodes. Then FC_2 is fully connected to a sequential layer FC_3 comprising c number of nodes, where c is the number of classes. Finally, a softmax layer [45] is added to obtain the classified output.

Implementation details: In our DenserNet, an image of size 224×224 is fed as an input. Here, all the convolutional layers use the *same* convolutions, i.e., the input and output of a convolutional layer are of the same dimension. For our study undertaken in this paper, we use five dense blocks in total, and four layers in each of the dense blocks. In dense blocks, we use dropout with a rate of 20% at the end of every composite function G_l. It helps in preventing the overfitting problem.

The hyper-parameter k is set as 32. Therefore, the feature map f_1 has 32 number of channels, each of size $112 \times 112\left(=\frac{224}{2} \times \frac{224}{2}\right)$, which we represent as f_1: 112×112@32. Similarly, the feature maps f_2, f_3, f_4, and f_5 can be represented as f_2: 56×56@64, f_3: 28×28@128, f_4: 14×14@256, and f_5: 7×7@512, respectively. Thus, after the fifth dense block, we obtain feature map f_5 containing 512 $\left(=2^{5-1}.32\right)$ number of channels, each of size 7×7. Now, f_5 is fed to the avg pool layer, where the employed filter is of size 7×7. As a matter of fact, FC_1 layer contains 512 number of nodes. For FC_2, we fix the number of nodes as $h = 128$. In FC_3, the number of nodes c is decided based on the task undertaken, e.g., for the binary classification task, $c = 2$.

5. Experiments and discussions

In this section, we discuss the experimental study and analyze the efficacy of our system. To perform the experiments, we required a database containing radiological images. For this purpose, we gathered some publicly available databases. The database employed is discussed below followed by the performance evaluation of our proposed method.

5.1 Database employed

For experimental analysis, we employed two separate databases containing chest X-ray and thorax CT-scan images. The details of these databases are as follows.

(i) ***X-ray database*** **(D_X)*:*** This database (say, D_X) contains a large collection of chest X-ray images of several human-beings of various demographics. The total count of X-ray images in D_X is 6116 (=1576 + 2777 + 270 + 1493). In D_X, the pneumonia-affected image count is 4540 (=2777 + 270 + 1493), and normal image count is 1576. The pneumonia images are categorized into two groups, i.e., bacteria and virus, which contains 2777 and 1763 (=270 + 1493) number of images, respectively. The virus-affected images are further divided into two categories, i.e., COVID-19 versus non-COVID-19 X-ray images, which consist of 270 and 1493 number of samples, respectively. In Fig. 11.4, we pictorially represent this categorization.

The X-ray images are collected from some publicly available data repositories mentioned as follows. The normal, bacterial pneumonia, and non-COVID-19 viral pneumonia X-ray images are gathered from Ref. [47]. The COVID-19 viral pneumonia-affected X-ray images are collected from Ref. [48]. We only used the frontal chest X-ray images for our experimentation. In Fig. 11.5, we present some examples from D_X.

The training set of D_X contains 1342, 2535, 199, and 1345 number of samples of normal, bacteria, COVID-19, and non-COVID-19 categories, respectively. The details of the training, validation, and test sets of D_X are presented in Table 11.1.

(ii) ***CT scan database*** **(D_{CT}):** This database (say, D_{CT}) contains CT-scan images of human thorax. D_{CT} contains a total of 746 (= 349 + 397) number of CT-scan images of human thorax. In D_{CT}, the count of COVID-19–affected images is 349, and the count

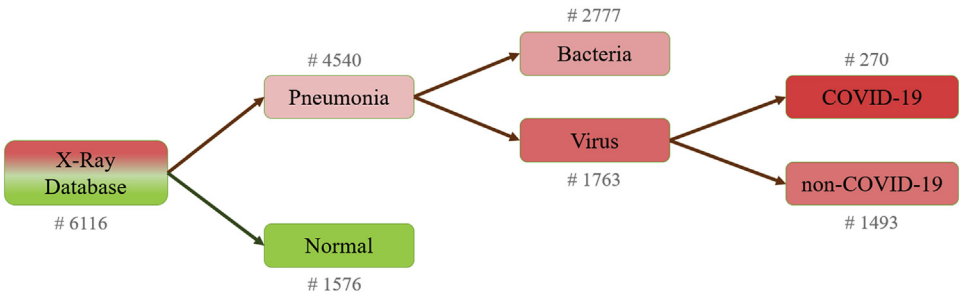

FIGURE 11.4 Medical image categories of X-ray database D_X with sample count (#).

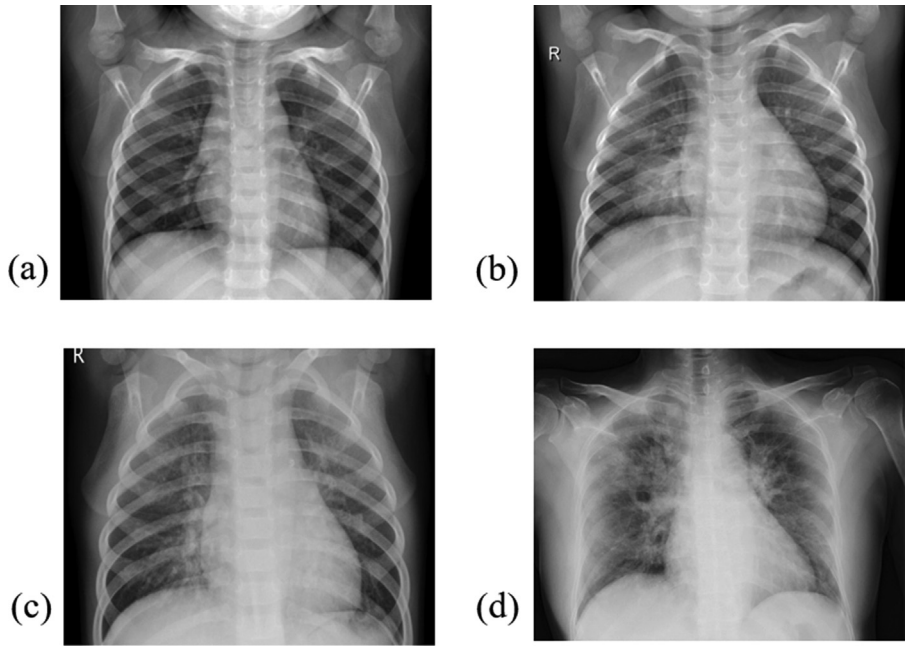

FIGURE 11.5 Examples from D_X database: (a) normal, (b) bacterial pneumonia, (c) non-COVID-19 viral pneumonia, (d) COVID-19 viral pneumonia.

Table 11.1 Training, validation, and test set distribution of D_X.

Category	Training	Validation	Test	Total
Normal	1342	46	188	1576
Bacteria	2535	48	194	2777
COVID-19	199	15	56	270
Non-COVID-19	1345	28	120	1493
Virus (COVID-19 + non-COVID-19)	1544	43	176	1763
Pneumonia (Bacteria + virus)	4079	91	370	4540

of non-COVID-19 images is 397. The samples of D_{CT} are obtained from a publicly available collection [49]. In Fig. 11.6, we present a pair of samples from D_{CT}.

The dataset D_{CT} is divided into training, validation, and test set as presented in Table 11.2.

5.2 Experimental results

In this subsection, we present the performance of our system carried out on databases D_X and D_{CT}. Here, we undertake various tasks to analyze bacterial pneumonia, viral pneumonia, and pandemic COVID-19.

Table 11.2 Training, validation, and test set distribution of D_{CT}.

Category	Training	Validation	Test	Total
COVID-19	219	36	94	349
Non-COVID-19	259	40	98	397

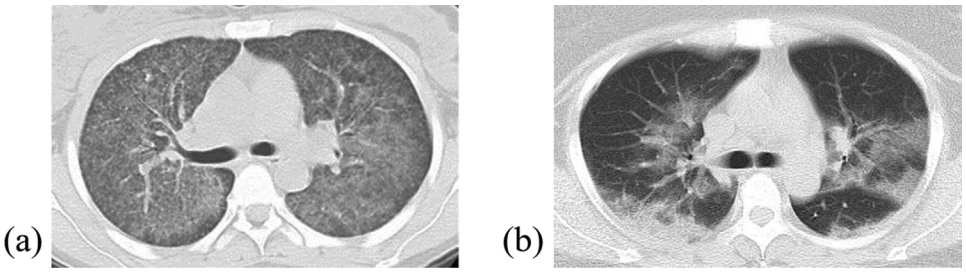

FIGURE 11.6 Examples from D_{CT} database: (a) non-COVID-19 and (b) COVID-19.

The tasks are mostly formulated as classification problems as below.

- **Task-1:** In this task, we perform a binary classification to classify the X-ray images of normal and pneumonia-affected patients.
- **Task-2:** Here, we classify the X-ray images of bacterial and viral pneumonia-affected patients.
- **Task-3:** In this task, the viral COVID-19–affected patients are separated from viral non-COVID-19 patients with respect to the X-ray images.
- **Task-4:** This task comprises the classification of four classes of X-ray images, i.e., normal, bacteria, viral COVID-19, and viral non-COVID-19.

  For Tasks 1, 2, 3, and 4, we use the X-ray images of D_X database.
- **Task-5:** Here, we perform a binary classification to detect COVID-19 and non-COVID-19 CT-scan images of D_{CT} database.

With respect to these five tasks, we train five models by employing the corresponding training sets as mentioned in Tables 11.1 and 11.2. At first, we train our DenserNet model for Task-4, then transfer the weights of the initial two dense blocks to the models for Task-1, Task-2, and Task-3. Here, we adopt the idea of transfer learning.

The training details of the models are mentioned as follows.

Training details: To tackle the overfitting problem, we employ data augmentation [50] with shear_range = 0.2, zoom_range = 0.2, brightness_range = [0.2,1.0], horizontal_flip = True, rotation_range = 30. All our models were trained using Adam optimizer [51] with mini-batch of size 64. Here, we fixed some hyper-parameters such as learning rate $(\alpha) = 0.01$, weight_decay $= 10^{-4}$, $\beta_1 = 0.9$, $\beta_2 = 0.999$, $\varepsilon = 10^{-8}$. We trained our models for 500 epochs. We did not use any early stopping [52]. We employed cross-entropy [52] as a loss function.

Table 11.3 Performance of DenserNet on various tasks.

Database	Task	Accuracy (%)	Precision (%)	Recall (%)	F_1 score (%)
D_X	Task-1	89.26	87.89	89.40	88.64
	Task-2	86.85	86.12	86.34	86.23
	Task-3	96.18	96.26	95.46	95.86
	Task-4	82.40	82.15	81.79	81.97
D_{CT}	Task-5	87.19	87.10	86.94	87.02

We measured the performance of our system in terms of accuracy, precision, recall, and F_1 score. The performance measures of our tasks are shown in Table 11.3.

From Table 11.3, we can note that our method performed the best for Task-3 by attaining 96.18% accuracy, where the task was to separate the viral COVID-19–affected patients from the viral non-COVID-19 patients with respect to the X-ray images.

On database D_X, our system obtained the lowest 82.40% accuracy for Task-4, where we classified into four classes of X-ray images, i.e., normal, bacteria, viral COVID-19, and viral non-COVID-19.

For Task-1 and Task-2, we obtained 89.26% and 86.85% accuracies, respectively.

On database D_X, the highest to lowest performances of the tasks are in the following order: Task-3 > Task-1 > Task-2 > Task-4.

On database D_{CT}, we executed only Task-5, where we obtained 87.19% accuracy for detecting COVID-19 versus non-COVID-19 with respect to CT-scan images.

In Table 11.3, we observe a similar trend with respect to the F_1 score. The highest F_1 score was achieved for Task-3, and the lowest F_1 score was attained for Task-4.

Fig. 11.7 shows the bar chart representation of our DenserNet performance over the five tasks in terms of accuracy.

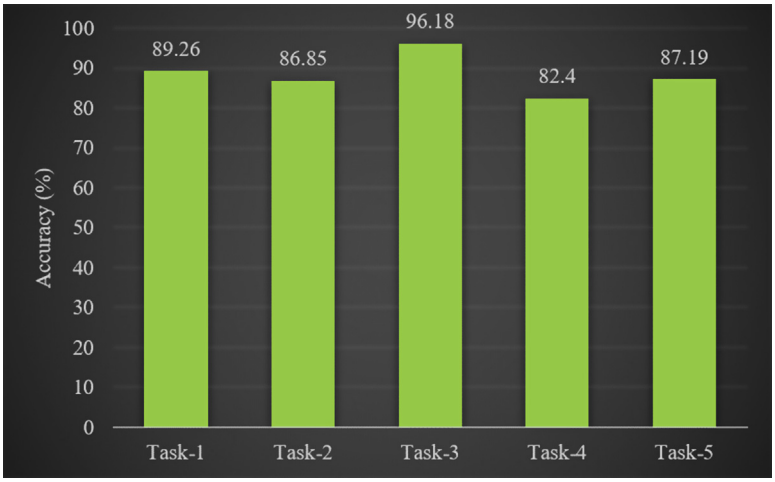

FIGURE 11.7 Bar chart representation of DenserNet performance on various tasks.

5.3 Comparison

We compared our proposed DenserNet architecture with some state-of-the-art deep learning-based architectures, such as GoogLenet [53], VGG-16 [54], ResNet-101 [46], and DenseNet [27] that work well on ImageNet database [55].

For a fair comparison, all the architectures were trained on the same training data and a similar experimental setup. In Table 11.4, we present this comparison analysis with respect to the accuracy measure.

From Table 11.4, we can observe, overall, our DenserNet performed the best on databases D_X and D_{CT} with respect to the five undertaken tasks. This can be easily observed from the bar chart of Fig. 11.8. Overall, for all the tasks, the highest to lowest performances are as follows:

DenserNet > DenseNet > ResNet-101 > VGG-16 > GoogLenet.

Table 11.4 Comparison with state-of-the-art methods on D_X and D_{CT}.

		Accuracy (%)				
Database	**Task**	**GoogLenet**	**VGG-16**	**ResNet-101**	**DenseNet**	**DenserNet**
D_X	Task-1	81.76	82.65	85.45	87.75	89.26
	Task-2	79.34	81.14	84.30	85.28	86.85
	Task-3	87.74	88.39	91.76	94.53	96.18
	Task-4	74.15	75.33	79.27	81.52	82.40
D_{CT}	Task-5	81.06	81.79	84.65	85.73	87.19

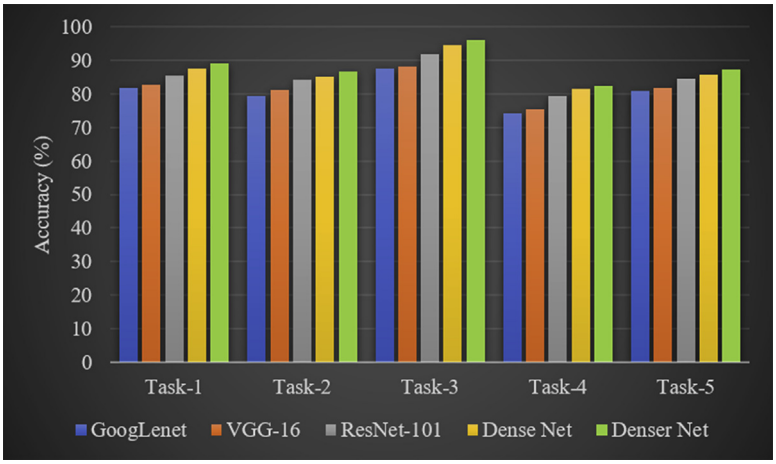

FIGURE 11.8 Bar chart for comparative analysis.

5.4 Research impact

Our method can be impactful in such a geographic location, where the proper COVID-19 test kit is not available, whereas the availability of an X-ray/CT-scan facility is there. In addition, our system has minimal human intervention, which is quite advantageous for breaking the chain of COVID-19 spread.

Moreover, our work can be extended to inspect some other medical images related to tuberculosis, tumor, bone fracture, etc.

6. Conclusion

In the present scenario, the whole world is facing a pandemic situation because of a massive outbreak of beta coronaviruses, specifically SARS-CoV-2 (COVID-19). In this paper, we work on analyzing COVID-19–affected medical images. For this purpose, we propose a densely connected deep CNN, named as DenserNet. We employ two publicly available databases D_X and D_{CT}, which contain chest X-ray and thorax CT scan images, respectively. For COVID-19 versus non-COVID-19 medical image separation, our DenserNet achieved 96.18% and 87.19% accuracies on databases D_X and D_{CT}, respectively.

In the future, we will endeavor to collaborate with some medical establishment to obtain more data, so that our system can learn various facets to produce better results. Currently, our system is mainly trained in analyzing COVID-19–affected medical images. However, our system can be extended to analyze some other medical images concerning tumor, tuberculosis, etc.

References

[1] C. Huang, Y. Wang, X. Li, L. Ren, J. Zhao, Y. Hu, et al., Clinical features of patients infected with 2019 novel coronavirus in Wuhan, China, Lancet 395 (10223) (Feb. 2020) 497–506.

[2] S. Jiang, Z. Shi, Y. Shu, et al., A distinct name is needed for the new coronavirus, Lancet 395 (10228) (Mar., 2020) P949.

[3] N. Zhu, D. Zhang, W. Wang, et al., A novel coronavirus from patients with pneumonia in China, N. Engl. J. Med. 382 (2020) 727–733.

[4] COVID-19 Dashboard by the Center for Systems Science and Engineering (CSSE) at Johns Hopkins University (JHU), ArcGIS, Johns Hopkins University. Retrieved from: 18 May 2020.

[5] S.R. Dubey, S.K. Singh, R.K. Singh, Local wavelet pattern: a new feature descriptor for image retrieval in medical CT databases, IEEE Trans. Image Process. 24 (12) (2015) 5892–5903.

[6] F. Li, W. Li, Y. Shu, S. Qin, B. Xiao, Z. Zhan, Multiscale receptive field based on residual network for pancreas segmentation in CT images, Biomed. Signal Process Contr. 57 (2020).

[7] Z. Chen, X. Wang, K. Yan, J. Zheng, Deep multi-scale feature fusion for pancreas segmentation from CT images, Int. J. Comput. Assist. Radiol. Surg. 15 (3) (2020) 415–423.

[8] N. Feng, X. Geng, L. Qin, Study on MRI medical image segmentation technology based on CNN-CRF model, IEEE Access 8 (2020) 60505–60514.

[9] Y. Huang, P. Singh, H. Kuo, A hybrid fuzzy clustering approach for the recognition and visualization of MRI images of Parkinson's disease, IEEE Access 8 (2020) 25041−25051.

[10] J. Kang, W. Lu, W. Zhang, Fusion of brain PET and MRI images using tissue-aware conditional generative adversarial network with joint loss, IEEE Access 8 (2020) 6368−6378.

[11] T.M. Carreras, C.E. Kahn Jr., Integrating Wikipedia articles and images into an information resource for radiology patients, J. Digit. Imag. 32 (3) (2019) 349−353.

[12] M.A. Nogueira, P.H. Abreu, P. Martins, P. Machado, H. Duarte, J. Santos, Image descriptors in radiology images: a systematic review, Artif. Intell. Rev. 47 (4) (2017) 531−559.

[13] M. Yamaghani, F. Zargari, Classification and retrieval of radiology images in H.264/AVC compressed domain, Signal Image Video Process. 11 (3) (2017) 573−580.

[14] S. Loveymi, M.H. Dezfoulian, M. Mansoorizadeh, Generate structured radiology report from CT images using image annotation techniques: preliminary results with liver CT, J. Digit. Imag. 33 (2) (2020) 375−390.

[15] H. Li, H. Jiang, S. Li, M. Wang, Z. Wang, G. Lu, J. Guo, Y. Wang, DenseX-Net: an end-to-end model for lymphoma segmentation in whole body PET/CT images, IEEE Access 8 (2020) 8004−8018.

[16] X. Li, Y. Guo, F. Jiang, L. Xu, F. Shen, Z. Jin, Y. Wang, Multi-task refined boundary-supervision U-Net (MRBSU-Net) for gastrointestinal stromal tumor segmentation in endoscopic ultrasound (EUS) images, IEEE Access 8 (2020) 5805−5816.

[17] M.N. Luong, Y. Shimada, K. Araki, M. Yoshiyama, J. Tagami, A. Sadr, Diagnosis of occlusal caries with dynamic slicing of 3D optical coherence tomography images, Sensors 20 (6) (2020) 1659.

[18] S. Ghoshal, P. Chatterjee, S. Banu, A. Chakrabarti, E.E. Mangina, A software tool for 3D visualization and slicing of MR images, in: Proc. Int. Conf. on Simulation Tools and Techniques, ACM, 2017, pp. 103−107.

[19] C. Perra, D.D. Giusto, JPEG 2000 compression of unfocused light field images based on lenslet array slicing, in: IEEE International Conference on Consumer Electronics, ICCE, IEEE, 2017, pp. 27−28.

[20] T. Manojlovic, D. Ilic, D. Miletic, I. Stajduhar, Using DICOM tags for clustering medical radiology images into visually similar groups, in: Int. Conf. on Pattern Recognition Applications and Methods (ICPRAM), 2020, pp. 510−517.

[21] F. Kruggel, A simple measure for acuity in medical images, IEEE Trans. Image Process. 27 (11) (2018) 5225−5233.

[22] J. Zhang, M. Liu, D. Shen, Detecting anatomical landmarks from limited medical imaging data using two-stage task-oriented deep neural networks, IEEE Trans. Image Process. 26 (10) (2017) 4753−4764.

[23] R. Nichenametla, T. Maneesha, S. Hafeez, H. Krishna, Prediction of heart disease using machine learning algorithms, Int. J. Eng. Technol. 7 (05 2018) 363−366.

[24] W. Ausawalaithong, S. Marukatat, A. Thirach, T. Wilaiprasitporn, Automatic Lung Cancer Prediction from Chest X-Ray Images Using Deep Learning Approach, Biomedical Engineering International Conference (BMEiCON), 2018.

[25] B. Guan, G. Zhanga, J. Yao, X. Wang, M. Wanga, Arm fracture detection in X-rays based on improved deep convolutional neural network, Comput. Electr. Eng. 81 (January 2020).

[26] X. Chen, C. Zhang, Y. Liu, Bone age assessment with X-ray images based on contourlet motivated deep convolutional networks, in: Int. Workshop on Multimedia Signal Processing, 2018, pp. 1−6.

[27] G. Huang, Z. Liu, L. Van Der Maaten, K.Q. Weinberger, Densely Connected Convolutional Networks, CVPR, 2017, pp. 2261−2269.

[28] D. Lanz, A. Kaup, Graph-based compensated wavelet lifting for scalable lossless coding of dynamic medical data, IEEE Trans. Image Process. 29 (2020) 2439−2451.

[29] S. Zhou, D. Nie, E. Adeli, J. Yin, J. Lian, D. Shen, High-resolution encoder-decoder networks for low-contrast medical image segmentation, IEEE Trans. Image Process. 29 (2020) 461–475.

[30] M. Goyal, A. Oakley, P. Bansal, D. Dancey, M.H. Yap, Skin lesion segmentation in dermoscopic images with ensemble deep learning methods, IEEE Access 8 (2020) 4171–4181.

[31] M. Rahimzadeh, A. Attar, A New Modified Deep Convolutional Neural Network for Detecting COVID-19 from X-Ray Images, 2020. CoRR, vol. abs/2004.08052.

[32] F. Shan, Y. Gao, J. Wang, W. Shi, N. Shi, M. Han, Z. Xue, D. Shen, Y. Shi, Lung infection quantification of COVID-19 in CT images with deep learning, CoRR (2020) vol. abs/2003.04655.

[33] M. Barstugan, U. Ozkaya, S. Ozturk, Coronavirus (COVID-19) Classification Using CT Images by Machine Learning Methods, 2020 arXiv:2003.09424.

[34] L. Wang, A. Wong, COVID-Net: A Tailored Deep Convolutional Neural Network Design for Detection of COVID-19 Cases from Chest X-Ray Images, 2020 arXiv:2003.09871.

[35] A. Narin, C. Kaya, Z. Pamuk, Automatic Detection of Coronavirus Disease (COVID-19) Using X-Ray Images and Deep Convolutional Neural Networks, 2020 arXiv:2003.10849.

[36] I.D. Apostolopoulos, T. Bessiana, COVID-19: Automatic Detection from X-Ray Images Utilizing Transfer Learning with Convolutional Neural Networks, 2020 arXiv:2003.11617.

[37] E.J. da S. Luz, P.L. Silva, R. Silva, G. Moreira, Towards an Effective and Efficient Deep Learning Model for COVID-19 Patterns Detection in X-Ray Images, 2020 arXiv:2004.05717.

[38] S.H. Kassani, P.H. Kassani, M.J. Wesolowski, K.A. Schneider, R. Deters, Automatic Detection of Coronavirus Disease (COVID-19) in X-Ray and CT Images: A Machine Learning-Based Approach, 2020 arXiv:2004.1064.

[39] G. Maguolo, L. Nanni, A Critic Evaluation of Methods for COVID-19 Automatic Detection from X-Ray Images, 2020 arXiv:2004.12823.

[40] S. Hu, Y. Gao, Z. Niu, Y. Jiang, L. Li, X. Xiao, M. Wang, E.F. Fang, W. Menpes-Smith, J. Xia, H. Ye, G. Yang, Weakly Supervised Deep Learning for COVID-19 Infection Detection and Classification from CT Images, 2020 arXiv:2004.06689.

[41] H.S. Maghdid, A.T. Asaad, K.Z. Ghafoor, A.S. Sadiq, M.K. Khan, Diagnosing COVID-19 Pneumonia from X-Ray and CT Images Using Deep Learning and Transfer Learning Algorithms, 2020 arXiv: 2004.00038.

[42] F. Shi, et al., Review of artificial intelligence techniques in imaging data acquisition, segmentation and diagnosis for COVID-19, IEEE Rev. Biomed. Eng., 14, 4-15 (2021) https://doi.org/10.1109/RBME.2020.2987975, (in print).

[43] Y. LeCun, L. Bottou, Y. Bengio, P. Haffner, Gradient-based learning applied to document recognition, Proc. IEEE 86 (11) (Nov. 1998) 2278–2324.

[44] S. Ioffe, C. Szegedy, Batch Normalization: Accelerating Deep Network Training by Reducing Internal Covariate Shift, ICML, 2015, pp. 448–456.

[45] M.Z. Alom, et al., The History Began from AlexNet: A Comprehensive Survey on Deep Learning Approaches', 2018 arXiv:1803.01164.

[46] K. He, X. Zhang, S. Ren, J. Sun, Deep residual learning for image recognition, in: Proc. CVPR, June 2016, pp. 770–778.

[47] D.S. Kermany, et al., Identifying medical diagnoses and treatable diseases by image-based deep learning, Cell 172 (5) (2018) 1122–1131.

[48] J.P. Cohen, P. Morrison, L. Dao, COVID-19 Image Data Collection, 2020 arXiv:2003.11597.

[49] J. Zhao, Y. Zhang, X. He, P. Xie, COVID-CT-Dataset: A CT Scan Dataset about COVID-19, 2020 arXiv: 2003.13865.

[50] L. Perez, J. Wang, The Effectiveness of Data Augmentation in Image Classification Using Deep Learning, 2017 arXiv:1712.04621.

[51] D.P. Kingma, J.L. Ba, Adam: A Method for Stochastic Optimization, 2014 arXiv:1412.6980v9.

[52] I. Goodfellow, Y. Bengio, A. Courville, Deep Learning, MIT Press, 2016.

[53] C. Szegedy, et al., Going Deeper with Convolutions, 2014 arXiv:1409.4842.

[54] K. Simonyan, A. Zisserman, Very Deep Convolutional Networks for Large-Scale Image Recognition, 2014 arXiv:1409.1556.

[55] O. Russakovsky, et al., ImageNet large scale visual recognition challenge, Int. J. Comput. Vis. 115 (3) (December 2015) 211−252.